IEEE Open Journal of
Power Electronics

Received 9 July 2024; revised 2 August 2024; accepted 12 August 2024. Date of publication 15 August 2024;
date of current version 6 September 2024. The review of this article was arranged by Associate Editor Tommaso Caldognetto.

Digital Object Identifier 10.1109/OJPEL.2024.3443921

Measurement of Inductive Power Transfer Coupling Pad Stress by Reconfiguring the Double-Sided-LCC Topology in a Limited Laboratory Environment

SEUNGJIN JO [1], GUANGYAO LI [2], JUNCHEN XIE [1] (Member, IEEE), AND DONG-HEE KIM [1] (Member, IEEE)

[1]Department of Electrical Engineering, Chonnam National University, Gwangju 61186, Korea
[2]Harbin Institute of Technology Zhengzhou Research Institute, Zhengzhou 450007, China

CORRESPONDING AUTHOR: DONG-HEE KIM (e-mail: kimdonghee@jnu.ac.kr).

This work was supported in part by the Korea Institute of Energy Technology Evaluation and Planning (KETEP) under Grant RS-2023-00281219.

ABSTRACT This paper proposes a process for measuring the rated power electrical characteristics of inductive power transfer (IPT) coupling pads in limited laboratory environments through topology reconfiguration. Among the components of IPT systems, the coupling pad is responsible for the main losses in the converter. Moreover, coupling pads have nonlinear characteristics that depend on various factors, such as the number of coil turns, the diameter, the permeability of the magnetic material, and the amount of aluminum. Therefore, verifying the operation is necessary when applying various position and control algorithms after configuring an IPT system. The input/output characteristics of the IPT system are mainly determined by the coupling pad and the employed compensation topology. Verifying the operation of the coupling pad becomes challenging when the IPT application's required input/output characteristics exceed the experimental voltage range in laboratory environments. The same electrical stress is applied to the coupling pad through topology reconfiguration and resonance component tuning, and the input/output characteristics can be flexibly changed to present a guideline that can be tested in a laboratory environment. A 3-resonance component circuit allows for modeling various compensation topologies. The same electrical and heating stress are verified through a 3.3-kW experimental prototype.

INDEX TERMS Compensation topology, experimental testing, inductive power transfer (IPT), measurement.

I. INTRODUCTION

Inductive power transfer (IPT) is a non-contact electrical energy transfer method that is used in various applications [1], [2], [3], [4], [5] because IPT systems have the advantages of safety and convenience compared to conventional wired charging methods [6], [7]. The IPT systems are used to charge batteries with wide output voltage characteristics, although they require a wide range of input/output specifications to control and compensate for power derating due to air gap fluctuations [8], [9], [10], [11].

The component that has the greatest impact on the losses of IPT systems is the coupling pad, which is composed of litz wires, magnetic materials, and aluminum plates for magnetic shielding [12]. Since most coupling pads have a low coupling coefficient of less than 0.5 between the primary and secondary pads [2], more current flows through the pads than high coupling coefficient transformers to transfer same energy. High current causes coupling pad loss and heat generation problems, and high voltage stress applied by high current can lead to insulation breakdown problems between coil turns and magnetic materials as shown in Fig. 1. Therefore, when conducting the IPT system, it should be designed by considering the coupling pad stress.

Different with transformers with high coupling coefficients, coupling pad with low coupling coefficients exhibits significant leakage flux in the surrounding air as shown in Fig. 2. Fig. 2(a) illustrates finite element method (FEM) of the transformer with a small air gap inside, indicating minimal leakage

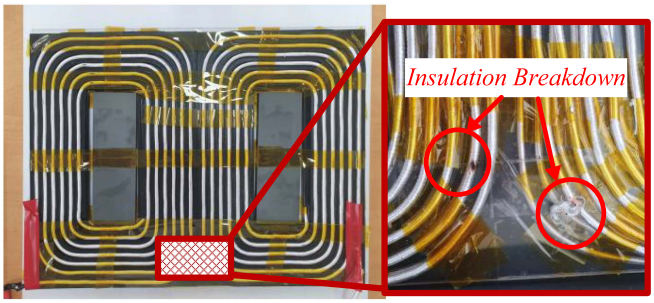

FIGURE 1. Voltage insulation breakdown coupling pad.

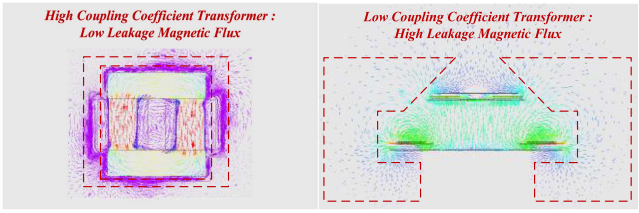

FIGURE 2. FEM magnetic flux simulation (a) transformer and (b) coupling pad.

flux and facilitating ease of magnetic circuit analysis. On the other hand, Fig. 2(b) depicts the coupling pad with a wide air gap between the primary and secondary sides. Considering various factors such as the length of the coils constituting the pad, winding methods, inner and outer diameters, permeability of magnetic materials, volume, iron loss characteristics, and differences in size between pads, there are challenges in accurately deriving coupling pad losses.

Numerous studies have been undertaken to model and optimize coils, magnetic materials, and the arrangement of aluminum plates in coupling pads aiming to enhance efficiency and achieve accurate derivation of loss characteristics in IPT systems [13], [14], [15], [16], [17], [18], [19], [20]. [13], [14], [15], [16]. propose the method of calculating coil AC resistance and loss through mathematical analysis. [17], [18] derive and propose optimal values by repetitive FEM simulations, and [19] propose to derive optimal efficiency by measuring and comparing each actual coil winding. [20] proposes iron loss calculation by calculating the properties of magnetic materials. However, accurate losses have not been derived through a formula that considers all the nonlinear characteristics of the coil, magnetic material, and aluminum plate constituting the coupling pad. In FEM simulations, obtaining accurate loss values demands substantial computing resources, and discrepancies may arise when compared to the practical test results. Therefore, to verify the voltage/current stresses, electrical insulation, and heat generation applied to the coupling pad through charging operation tests must be conducted.

However, measurements on a coupling pad at the rated power are not always possible in a limited laboratory environment. Generally, IPT applications have a wide voltage gain characteristic. If the DC source or DC load specifications in the laboratory are insufficient compared to the IPT input/output requirements, the IPT full-load test would be difficult.

To satisfy the input/output requirements, the addition of DC/DC converters to the input side and the output side could be achieved. However, adding an auxiliary DC/DC converter with the same rated power as the IPT system would be costly and time-consuming. Accordingly, in limited laboratory environments, a method is required that enables verification of the rated power operation of coupling pad with minimal additional costs and time.

This paper proposes a method to meet input/output characteristics in a laboratory environment by reconfiguring the compensation topology of an existing IPT system to the double-sided LCC (DS-LCC) compensation topology, thereby applying the same electrical stresses to the coupling pad. Existing studies on topology reconfiguration have primarily focused on proposing solutions for output compensation by changing constant current/constant voltage modes and adjusting separation distances [21], [22]. However, this study proposes a novel approach from the perspective of measuring stress on the coupling pads.

First, the factors influencing coupling pad losses in IPT systems are derived, and the factors affecting pad losses when various compensation topologies are applied are calculated. The basis 3-resonance component circuit model is proposed for various compensation topologies generally employed in IPT systems, and equations for calculating electrical characteristics are developed. Subsequently, the DS-LCC topology is reconfigured to achieve flexible voltage gains while determining resonance component parameters to impose identical electrical stresses. The proposed DS-LCC topology reconfiguration method reduces the time and cost of manufacturing DC/DC converters for operational verification in a limited laboratory environment. By using DS-LCC topology reconfiguration method, measuring the maximum electrical stress during the rated operation of the coupling pad is possible. Furthermore, the proposed method allows for the measurement of coupling pad stresses occurring when compensation control algorithms for rated operation are applied under misalignment conditions. The FEM simulations and 3.3-kW class experimental tests are conducted. The results of FEM simulations and experiments confirm that when DS-LCC topology reconfiguration method is applied, same current stresses, losses, and temperature fluctuation occur on the coupling pad.

II. IPT COMPENSATION TOPOLOGY ANALYSIS

A. COUPLING PAD LOSS FACTORS

Prior to the DS-LCC topology reconfiguration method, an analysis of the factors influencing the electrical stress on the coupling pad is conducted. Fig. 3 illustrates the components

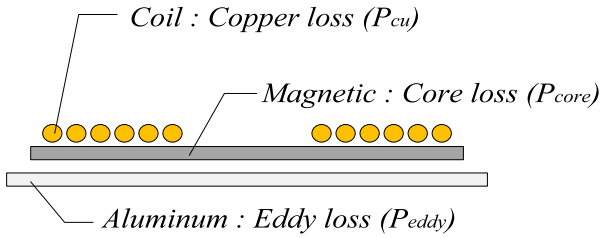

FIGURE 3. Coupling pad loss components.

comprising the coupling pad and the associated loss factors. The losses include copper losses from the coils, core losses from the magnetic materials, and eddy current losses from the aluminum plate. The losses in the coupling pad are presented in (1)–(3), where P_{cu}, P_{core}, and P_{eddy} are the total copper losses, core losses, and eddy current losses, respectively. R_{dc} is the DC resistance. R_{skin}, R_{prox} represent the skin effect resistance and proximity effect resistance, respectively, which have a significant component when high-frequency currents flow [23]. B_{ac}, B_m are AC flux density, and maximum flux density, respectively. K_{fe}, α, and β are core material coefficient [24]. t is thickness of lamination, f is frequency, V is volume of the material. K_{eddy} is eddy current constant.

$$P_{cu} = I^2(R_{dc} + R_{skin} + R_{prox}). \tag{1}$$

$$P_{core} = K_{fe} f^{\alpha} {B_{ac}}^{\beta}. \tag{2}$$

$$P_{eddy} = K_{eddy} t^2 f^2 {B_m}^2 V. \tag{3}$$

Most of the factors that establish the losses of the coupling pad are determined when the pad design is completed. (1)–(3) show the electrical factors that the total coupling pad loss is determined by the current magnitude and frequency.

B. EQUIVALENT CIRCUIT MODELING FOR ANALYZING COUPLING PAD ELECTRICAL STRESSES

The AC equivalent circuit modeling of the IPT system is conducted to derive the current magnitude and frequency components that affect the loss of coupling pads. Fig. 4(a) presents a schematic diagram of the IPT system, which comprises a full-bridge inverter (FBI), a resonant compensation network, and a single-phase full-bridge rectifier (SBR).

The FBI is composed of four power MOSFETs Q_1–Q_4 and is used to convert the DC-link voltage U_{DC} to the AC voltage U_{AB}. Generally, U_{AB} is assumed to be a square wave with a fixed duty cycle of 0.5 without dead time. The fundamental harmonic root mean square (RMS) value ($\boldsymbol{U}_{AB}$) is derived as follows:

$$U_{AB} = \left|\dot{U}_{AB}\right| = \frac{2\sqrt{2}}{\pi} U_{DC}. \tag{4}$$

The AC power that is converted through the FBI is transmitted through a loosely coupled transformer (LCT), which comprises transmitting and receiving coils. L_i and R_i ($i = p, s$) are the self-inductances and parasitic resistance of the LCT

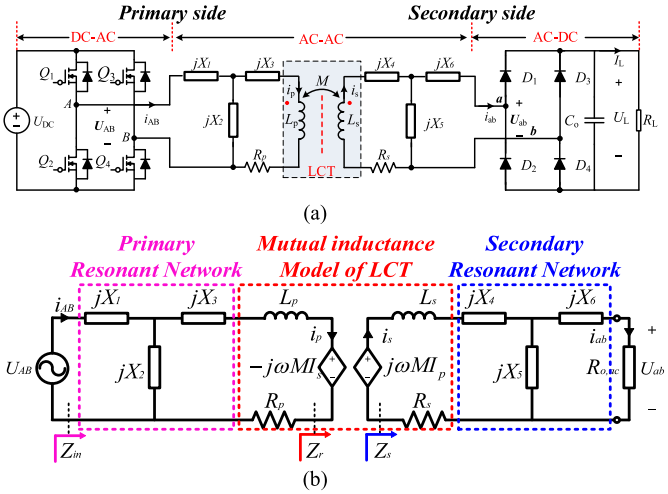

FIGURE 4. (a) IPT system. (b) Mutual-inductance and 3-resonance component basis circuit model of the compensation topology.

parameters on the primary (p) and secondary (s), respectively. M is the mutual inductance of the two coils, and the coupling coefficient k is defined as follows:

$$k = \frac{M}{\sqrt{L_p L_s}}. \tag{5}$$

The SBR comprises four power diodes (D_1–D_4) and is used to regulate the AC output voltage to the DC battery voltage. The output low-pass filter contains an output filter capacitor C_o, and the RMS values of the output AC and DC components have the following relationships [25]:

$$U_{ab} = \frac{\pi\sqrt{2}}{2} U_L,\ i_{ab} = \frac{2\sqrt{2}}{\pi} I_L. \tag{6}$$

where U_{ab} and i_{ab} are the RMS values of the AC output components. Based on (6), the relationship between an AC equivalent resistance $R_{o,ac}$ and the load resistance R_L can be deduced as:

$$R_{o,ac} = \frac{8}{\pi^2} R_L. \tag{7}$$

The FBI and SBR circuits in Fig. 4(a) can be replaced by an AC source and an AC equivalent load by (4) and (7), respectively. In addition, the LCT is considered equivalent to the mutual inductance model. Therefore, the analysis and calculations of the IPT system in Fig. 4(a) can be simplified by representing it as a mutual-inductance model-based analysis circuit, as displayed in Fig. 4(b).

Generally, the primary and secondary resonant networks are configured with up to three resonance compensation elements ($jX_1 - jX_6$). These 3-resonance components depicted in Fig. 4(b) are calculated according to the compensation topology selected for various IPT systems. The secondary side impedance Z_s in Fig. 4(b) is as follows:

$$Z_s = j\omega L_s + R_s + jX_4 + \frac{1}{\frac{1}{jX_5} + \frac{1}{jX_6 + R_{o,ac}}}. \tag{8}$$

TABLE 1. IPT Basic Compensation Topologies

	S-S	S-P	P-S	P-P
Figure	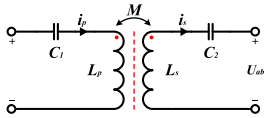	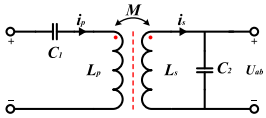	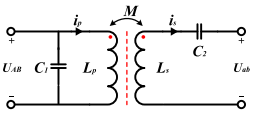	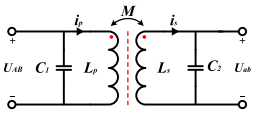
Resonant element status	$jX_1, jX_6 = 0, jX_2, jX_5 = \infty$ $jX_3 = \frac{1}{j\omega_r C_1}, jX_4 = \frac{1}{j\omega_r C_2}$	$jX_1, jX_4, jX_6 = 0, jX_2 = \infty$ $jX_3 = \frac{1}{j\omega_r C_1}, jX_5 = \frac{1}{j\omega_r C_2}$	$jX_1, jX_3, jX_6 = 0, jX_5 = \infty$ $jX_2 = \frac{1}{j\omega_r C_1}, jX_4 = \frac{1}{j\omega_r C_2}$	$jX_1, jX_3, jX_4, jX_6 = 0$ $jX_2 = \frac{1}{j\omega_r C_1}, jX_5 = \frac{1}{j\omega_r C_2}$
$Z_{in(\omega=\omega_r)}$	$\frac{(\omega_r M)^2}{R_{o,ac}}$	$\frac{(\omega_r M)^2}{j\omega_r L_s + \frac{R_{o,ac}}{1 + j\omega_r C_2 R_{o,ac}}}$	$\frac{1}{j\omega_r C_1 + \frac{R_{o,ac}}{j\omega_r L_p R_{o,ac} + (\omega_r M)^2}}$	$\frac{1}{j\omega_r C_1 + \frac{1}{j\omega_r L_p + \frac{(1 + j\omega_r C_2 R_{o,ac})(\omega_r M)^2}{j\omega_r L_s}}}$
i_p	$\frac{U_{AB} R_{o,ac}}{(\omega_r M)^2}$	$\frac{U_{AB} R_{o,ac}}{(\omega_r M)^2} \cdot \left(j\omega_r L_s + \frac{R_{o,ac}}{1 + j\omega_r C_2 R_{o,ac}} \right)$	$\frac{U_{AB}(j\omega_r C_p Z_s + 1)}{j\omega_r L_p + Z_s}$	$\frac{U_{AB}(j\omega_r C_p Z_s + 1)}{j\omega_r L_p + Z_s}$
i_s	$\frac{U_{AB}}{\omega_r M}$	$\frac{j\omega_r M U_{AB}}{\left(\frac{j\omega_r L_s}{1 + j\omega_r C_s R_{o,ac}} \right)^2}$	$\frac{j\omega_r M}{R_{o,ac}} \cdot \frac{U_{AB}(j\omega_r C_p Z_s + 1)}{j\omega_r L_p + Z_s}$	$\frac{j\omega_r M}{\left(\frac{j\omega_r L_s}{j\omega_r C_s R_{o,ac} + 1} \right)} \cdot \frac{U_{AB}(j\omega_r C_p Z_s + 1)}{j\omega_r L_p + Z_s}$
U_{ab}	$\frac{U_{AB} R_{o,ac}}{\omega_r M}$	$\frac{j\omega_r M U_{AB}}{\frac{(j\omega_r L_s)^2}{1 + j\omega_r C_s R_{o,ac}}}$	$\frac{j\omega_r M U_{AB}(j\omega_r C_p Z_s + 1)}{j\omega_r L_p + Z_s}$	$\frac{M}{L_s} \cdot \frac{U_{AB}(j\omega_r C_p Z_s + 1) R_{o,ac}}{j\omega_r L_p + Z_s}$

The reflected impedance converted from the secondary side to primary side is deduced as follows:

$$Z_r = \frac{(\omega M)^2}{Z_s}. \tag{9}$$

The total input impedance is derived as follows:

$$Z_{in} = jX_1 + \frac{1}{\frac{1}{jX_2} + \frac{1}{jX_3 + j\omega L_p + R_p + Z_r}}. \tag{10}$$

C. INPUT/OUTPUT CHARACTERISTICS BY RESONANCE NETWORK

$$i_p = \frac{jX_2}{jX_2 + jX_3 + j\omega L_p + R_p + Z_r} i_{AB}. \tag{11}$$

$$i_s = \frac{j\omega M i_p}{Z_s}. \tag{12}$$

$$i_{AB} = \frac{U_{AB}}{Z_{in}}. \tag{13}$$

$$i_{ab} = \frac{jX_6}{jX_4 + jX_5 + j\omega L_s + R_s + R_{o,ac}} i_s. \tag{14}$$

The equations for the current flowing in the IPT resonance circuit are expressed in (11)–(14), where i_p and i_s are the primary pad and secondary pad current, respectively. $jX_1 - jX_6$ are composed of inductors, capacitors, represented as short or open circuits.

Tables 1 and 2 specify the reactance values of each resonance compensation element, as well as impedance, current magnitude of the coupling pad, and output voltage when various compensation topologies are applied to the basis circuit model specified in Fig. 4(b). In addition to the compensation topologies specified in Table 1 and 2 [24], although various other topologies have been proposed [27], [28], [29], only some of these compensation topologies are attached as examples for simplicity. As shown in Tables 1 and 2, the output characteristics of the IPT converter depend on the specification of the coupling pad. Hence, the input/output range of the experimental prototype can exceed the operational range in the laboratory environment depending on the compensation topology and coupling pad characteristics when manufacturing the IPT system. In the subsequent section, the method for reconfiguring various compensation topologies, including Tables 1 and 2, into the DS-LCC topology is presented. By applying the reconfiguration method, the principle that enables the flexible design of voltage gains while maintaining the same electrical stress is explained under rated operating conditions, allowing for testing in the laboratory environment.

III. TOPOLOGY RECONFIGURATION FOR COUPLING PAD MEASUREMENT

A. BASIC ANALYSIS OF DS-LCC TOPOLOGY

Fig. 5 shows the DS-LCC topology, which is reconfigured from Fig. 4(b). The DS-LCC topology is a high-order topology in which one resonance inductor (L_{in1}, L_{in2}) and two resonance capacitors (C_{p1}, C_{p2}, C_{f1}, C_{f2}) are added to the primary and secondary sides, respectively. C_{p1} and C_{p2} are parallel capacitors, while C_{f1} and C_{f2} are series capacitors on the primary and secondary sides, respectively. U'_{AB}, i'_p, i'_s, and U'_{ab} are the input voltage, primary pad current, secondary pad current, and output voltage when reconfigured topology, respectively. The DS-LCC topology achieves electrical isolation through V-C conversion by incorporating an LC network between the input power side and the primary coupling pad,

TABLE 2. IPT High-Order Compensation Topologies

	LCL-S	LCC-S	LCL-P	LCC-P
Figure	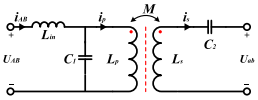	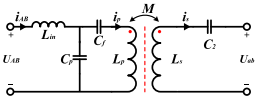	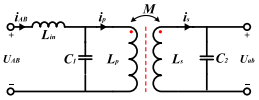	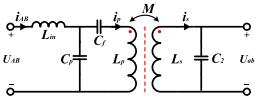
Resonant element status	$jX_3, jX_6 = 0,\ jX_5 = \infty,$ $jX_1 = j\omega_r L_{in}$ $jX_2 = \frac{1}{j\omega_r C_1}, jX_4 = \frac{1}{j\omega_r C_2}$	$jX_6 = 0, jX_5 = \infty$ $jX_1 = j\omega_r L_{in}$ $jX_5 = \frac{1}{j\omega_r C_2}$ $jX_2 = \frac{1}{j\omega_r C_p}, jX_3 = \frac{1}{j\omega_r C f_f}$	$jX_1, jX_3, jX_6 = 0, jX_5 = \infty$ $jX_2 = \frac{1}{j\omega_r C_1}, jX_4 = \frac{1}{j\omega_r C_2}$	$jX_1, jX_3, jX_4, jX_6 = 0$ $jX_2 = \frac{1}{j\omega_r C_1}, jX_5 = \frac{1}{j\omega_r C_2}$
$Z_{in(\omega=\omega_r)}$	$\frac{(\omega_r M)^2}{R_{o,ac}}$	$\frac{(\omega_r M)^2}{j\omega_r L_s + \frac{R_{o,ac}}{1 + j\omega_r C_2 R_{o,ac}}}$	$\frac{1}{j\omega_r C_1 + \frac{R_{o,ac}}{j\omega_r L_p R_{o,ac} + (\omega_r M)^2}}$	$\frac{1}{j\omega_r C_1 + \frac{1}{j\omega_r L_p + \frac{(1 + j\omega_r C_2 R_{o,ac})(\omega_r M)^2}{j\omega_r L_s}}}$
i_p	$\frac{U_{AB}}{j\omega_r L_p}$	$\frac{U_{AB}}{j\omega_r L_{in}}$	$\frac{U_{AB}}{j\omega_r L_p}$	$\frac{U_{AB}}{j\omega_r L_{in}}$
i_s	$\frac{MU_{AB}}{L_p R_{o,ac}}$	$\frac{MU_{AB}}{L_{in} R_{o,ac}}$	$\frac{MU_{AB}}{L_p} \cdot \frac{j\omega_r C_s R_{o,ac} + 1}{j\omega_r L_s}$	$\frac{MU_{AB}}{L_{in}} \cdot \frac{j\omega_r C_s R_{o,ac} + 1}{j\omega_r L_s}$
U_{ab}	$\frac{MU_{AB}}{L_p}$	$\frac{MU_{AB}}{L_{in}}$	$\frac{MU_{AB}}{L_p} \cdot \frac{R_{o,ac}}{j\omega_r L_s}$	$\frac{MU_{AB}}{L_{in}} \cdot \frac{R_{o,ac}}{j\omega_r L_s}$

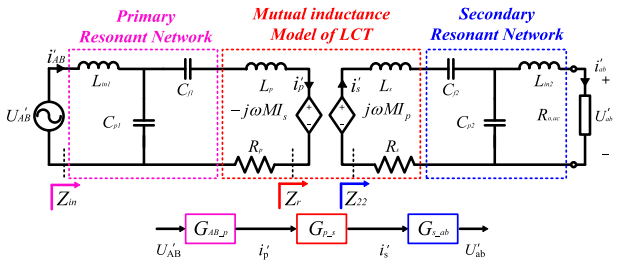

FIGURE 5. DS-LCC AC equivalent circuit reconfiguration.

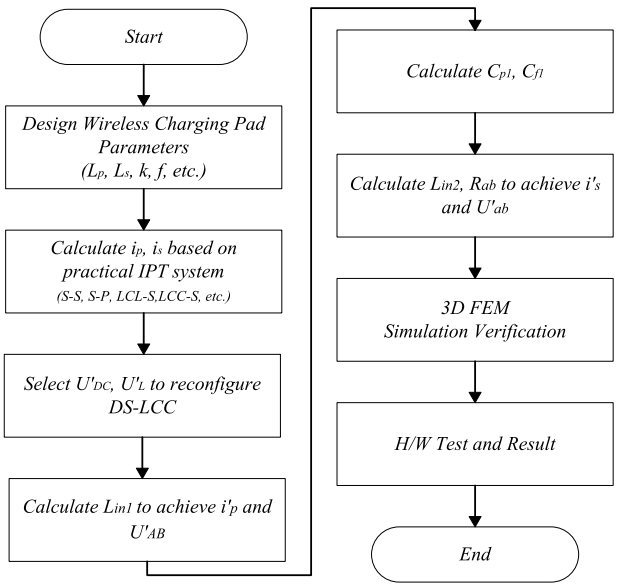

FIGURE 6. Design step of DS-LCC topology reconfiguration.

and between the secondary coupling pad and the output load [27]. This setup allows for effective electrical decoupling. Furthermore, by tuning C_{f1} and C_{f2}, the system can enable zero voltage switching (ZVS) operation [30]. Consequently, the relationship between the electrical stresses of the coupling pad and the input/output electrical characteristics can be flexibly designed. When operating at the resonance angular frequency ω_r, the impedance equation and the current flow through each loop, as determined by applying Kirchhoff's voltage law (KVL), are as follows:

$$\begin{cases} j\omega_r L_{in,i} + \frac{1}{j\omega_r C_{pi}} = 0 \\ \frac{1}{j\omega_r C_{pi}} + \frac{1}{j\omega_r C_{fi}} + j\omega_r L_i = 0 \end{cases} (i = 1(p), 2(s)). \tag{15}$$

$$\begin{cases} U'_{AB} = \left(j\omega L_{in1} + \frac{1}{j\omega C_{p1}}\right) i'_{AB} = \frac{1}{j\omega C_{p1}} i'_p \\ 0 = \left(j\omega L_{in2} + \frac{1}{j\omega C_{p2}} + R_{o,ac}\right) i'_{ab} - \frac{1}{j\omega C_{p2}} i'_s \\ 0 = \left(j\omega L_p + \frac{1}{j\omega C_{f1}} + \frac{1}{j\omega C_{p1}}\right) i'_p - \frac{1}{j\omega C_{p1}} i'_{AB} - j\omega M i'_s \\ 0 = \left(j\omega L_s + \frac{1}{j\omega C_{f2}} + \frac{1}{j\omega C_{p2}}\right) i'_s - \frac{1}{j\omega C_{p2}} i'_{ab} - j\omega M i'_p \end{cases} \tag{16}$$

B. DESIGN STEP OF DS-LCC TOPOLOGY RECONFIGURATION

Fig. 6 shows the design steps of the DS-LCC topology reconfiguration. First, the parameters of the coupling pad (which is manufactured for application in IPT systems) are measured. Next, based on the measured values of the coupling pad, the compensation topology for reducing the reactance component of the coupling pad is selected and designed. The input/output characteristics according to the topology and the current

flowing through the coupling pads are derived through calculations or formula calculations presented in Tables 1 and 2. After calculating the current flowing through the coupling pad, appropriate input/output voltage specifications are selected for a laboratory environment. The DS-LCC resonance parameter varies depending on the applicable voltage range. Based on the current flowing through the i'_1 and U'_{in}, L_{in1} is calculated as follows:

$$L_{in1} = \frac{U'_{in}}{j\omega_r i'_1}. \tag{17}$$

The L_{in2} value calculation, based on i'_2 and $U'_{o,ac}$, is as follows:

$$L_{in2} = \frac{U'_{o,ac}}{i'_2}\frac{1}{\omega_r R_{o,ac}}. \tag{18}$$

After deriving L_{in1} and L_{in2}, C_{p1}, C_{p2}, C_{f1}, and C_{f2} are determined based on (15). Therefore, the analysis and calculation of the IPT system displayed in Fig. 1(b) can be modified by reconfiguring it into a DS-LCC-based analysis circuit, as presented in Fig. 3. The gain equations for the input voltage, output voltage, and current flowing through the coupling pads are as follows:

$$G_{AB\_p} = \left|\frac{i'_p}{U'_{AB}}\right| = \frac{L_{in2}}{\omega_r{}^5 L_{in1} C_{p1}{}^2 C_{p2}{}^2 R_{o,ac}} = \frac{\omega_r L_{in1} L_{in2}{}^2}{R_{o,ac}}. \tag{19}$$

$$G_{p\_s} = \left|\frac{i'_s}{i'_p}\right| = \frac{\omega_r M}{Z_s} = \frac{\omega_r M C_{p2} R_{o,ac}}{L_{in2}} = \frac{M R_{o,ac}}{\omega_r L_{in2}{}^2}. \tag{20}$$

$$G_{s\_ab} = \left|\frac{U'_{ab}}{i'_s}\right| = \frac{1}{\omega_r C_{p2}} R_{o,ac} = \omega_r L_{in2} R_{o,ac}. \tag{21}$$

The currents in the DS-LCC topology are determined by the input AC voltage and the additional resonant inductors L_{in1} and L_{in2}. In a limited laboratory environment, the AC voltage range is limited. However, as shown in (15)–(18), the resonance inductors can be designed more flexibly than the coupling pad. The design of the DS-LCC resonance element allows the current flowing through the coupling pads of IPT systems with various compensation topologies to be measured while flexibly designing the input/output voltage specification. After reconfiguration, the rated operating state of the coupling pad is verified through a 3D simulation and an experimental test.

IV. EXPERIMENTAL VERIFICATION

A. IPT SYSTEM CONFIGURATION AND TEST POINT SELECTION

To verify the validity of the voltage/current stress measurements using the proposed DS-LCC topology reconfiguration method, an arbitrary IPT system was designed and a DS-LCC reconfiguration experiment was conducted. Two of the most popular topologies in the IPT system: the S-S topology, LCC-S topology were selected and reconfigured. In this paper, the S-S topology was selected and reconfigured. For the LCC-S topology, PSIM simulation in the appendix confirmed that it results in the same pad stress. In the S-S topology, the input/output and the coupling pad are connected in series. Hence, the characteristics of the coupling pad dominate the input/output characteristics.

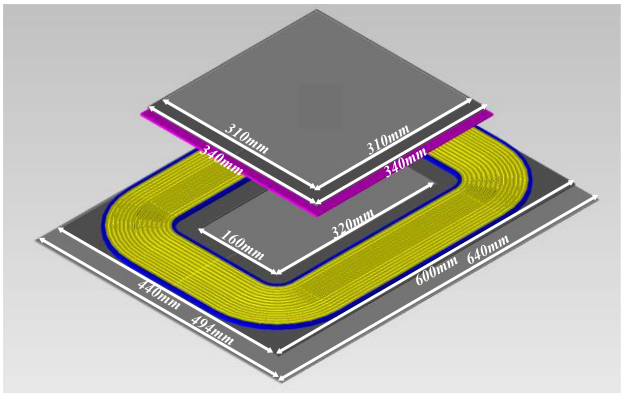

FIGURE 7. 3-D geometric IPT coupling pad and dimensions.

TABLE 3. Designed Dimensional Parameters of the LCT

Parameters	Values
Air gap distance range	100–150 mm
X and Y axial offset	0 mm
Turns per coil	N_p : 15, N_s : 19
Primary coil dimension	580 mm × 420 mm × 5 mm
Primary ferrite plate dimension	600 mm × 440 mm × 3 mm
Primary shield dimension	640 mm × 496 mm × 2 mm
Secondary coil dimension	320 mm × 320 mm × 5 mm
Secondary ferrite plate dimension	340 mm × 340 mm × 3 mm
Secondary shield dimension	310 mm × 310 mm × 2 mm
Litz wire coil specification	0.06mm/4200 strands
Ferrite material (Manufacturer)	PM12(todaisu)

TABLE 4. Essential Parameters of the IPT System

Symbols	Parameters	Values
f_r	Resonance frequency	100 kHz
P_o	Rated output power	3.3 kW
k	Coupling coefficient range	0.214
i_L	Output AC current	15 A
$L_{p,align}$	Primary coil inductance	213.2 μH
$L_{s,align}$	Secondary coil inductance	134.8 μH
M	Mutual inductance at z = 100mm	36.2 μH
	Mutual inductance at z = 150mm	25.6 μH
	Mutual inductance at x, y, z = 100mm	25.9 μH

Fig. 7 presents a 3-D geometric IPT pad manufactured based on the 3-D FEM simulation tool. The geometric characteristics of the 3-D IPT pad are specified in Table 3, which follows the size specifications for WPT systems as outlined in SAE J2954 Appendix F [31], and the electrical specifications are listed in Table 4. Fig. 8 shows the transconductance and input phase graphs according to the maximum/minimum k after designing the resonance capacitance of the S-S topology based on Table 4. The equation for the transconductance and

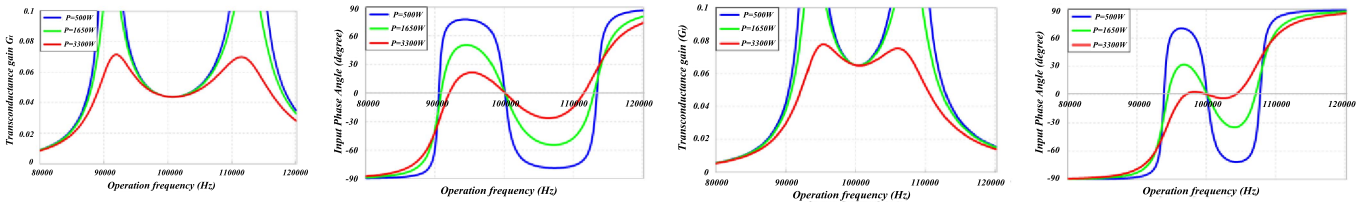

FIGURE 8. Phase-frequency and coupling pad frequency characteristics of the IPT system with S-S compensation topology under different R_L and k values: (a) $k = 0.214$. (b) $k = 0.145$.

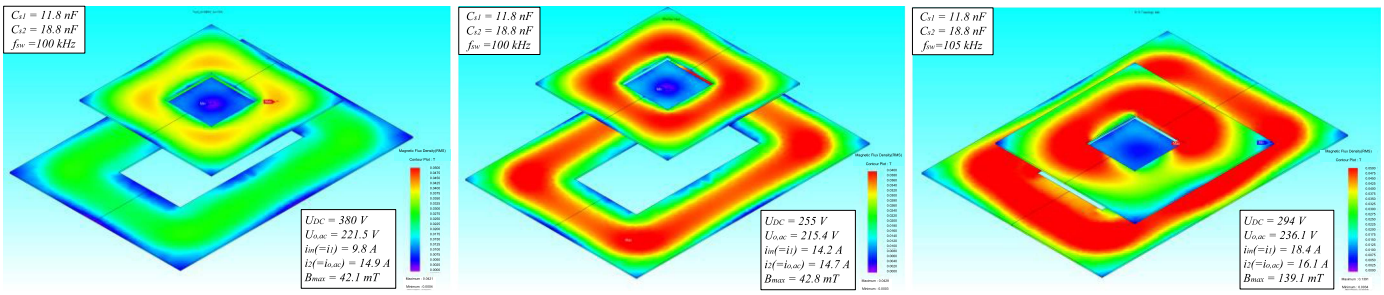

FIGURE 9. 3D FEM simulation results (S-S Topology) : (a) At $z = 100$ mm (align), (b) At $z = 150$ mm, and (c) at $x, y, z = 100$ mm.

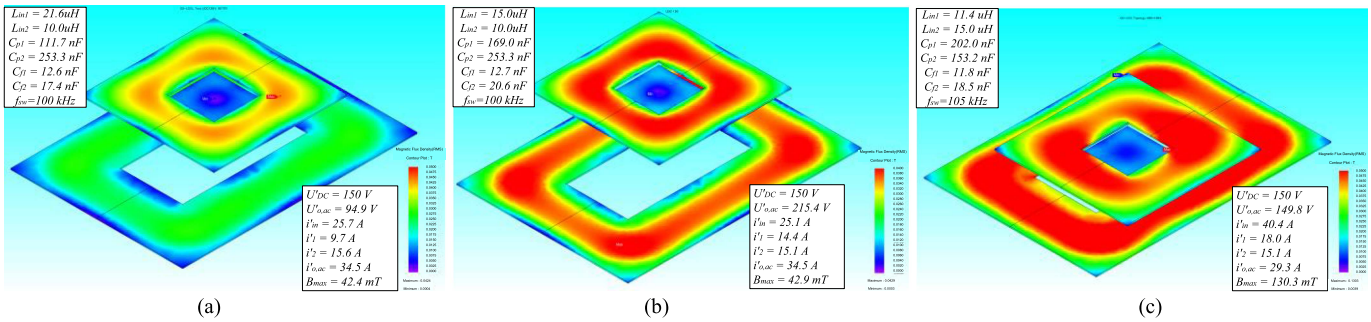

FIGURE 10. 3D FEM simulation results (DS-LCC Topology, $U_{DC} = 150$ V) : (a) At $z = 100$ mm (align), (b) At $z = 150$ mm, and (c) at $x, y, z = 100$ mm.

input phase is as follows:

$$G_t = \frac{i_{ab}}{U_{AB}}, \theta_{in} = \frac{180^\circ}{\pi}\tan^{-1}\frac{\mathrm{Im}(Z_{in})}{\mathrm{Re}(Z_{in})} \tag{22}$$

(22) shows the transconductance gain and the input phase angle. The input phase angle of the S-S topology depends on the coupling pad position, as specified in Fig. 8(b), which causes a reactance component and results in efficiency and durability reduction due to degradation. Therefore, when configuring a practical IPT system, a control algorithm for compensating input/output characteristics according to fluctuations in the inverter arm-shot problem as the phase is reversed to zero-current switching during operation, or an increase in separation distance between coupling pads is applied.

After selecting the compensation topology and control algorithm method to be configured in the IPT system, the validity of the proposed DS-LCC topology reconfiguration method was confirmed through simulations.

Figs. 9, 10, 11, and 12 display the results of the FEM simulations in the aligned and misaligned states, respectively, based on the IPT 3-D pad shown in Fig. 7. Fig. 9 shows the input/output characteristics, i_p, i_s, and maximum magnetic flux density results of the IPT system during the alignment state ($z = 100$ mm) and misalignment state ($z = 150$ mm, x, y, $z = 100$ mm) operation of the S-S topology, respectively. The misalignment distance range was selected considering the SAE J2954 standard [31]. For 3.3-kW rated operation in align state, the input voltage is selected so that the output AC current flows to 15 A. Fig. 9(a) is the result of the alignment simulation. The input voltage operated at 380 V. Fig. 9(b) is the simulation result at $z = 150$ mm, and the input voltage is operated at 255-V to keep the output rated power and output

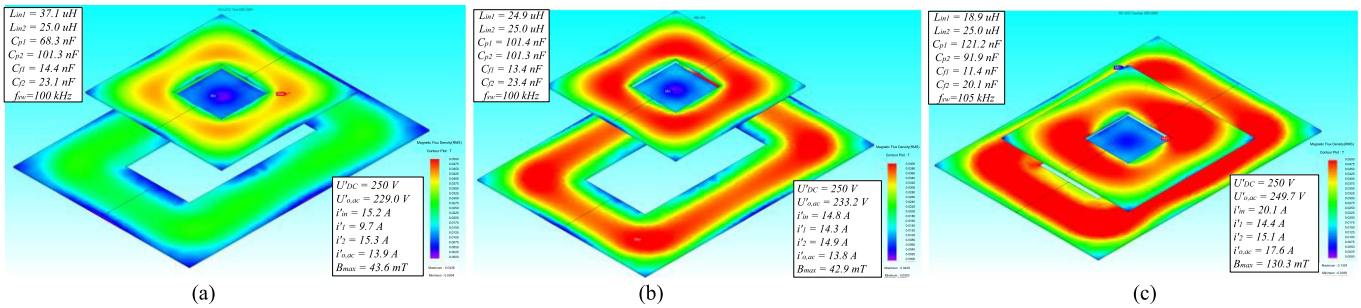

FIGURE 11. 3D FEM simulation results (DS-LCC topology, $U_{DC} = 250$ V) : (a) At $z = 100$ mm (align), (b) At $z = 150$ mm, and (c) at $x, y, z = 100$ mm.

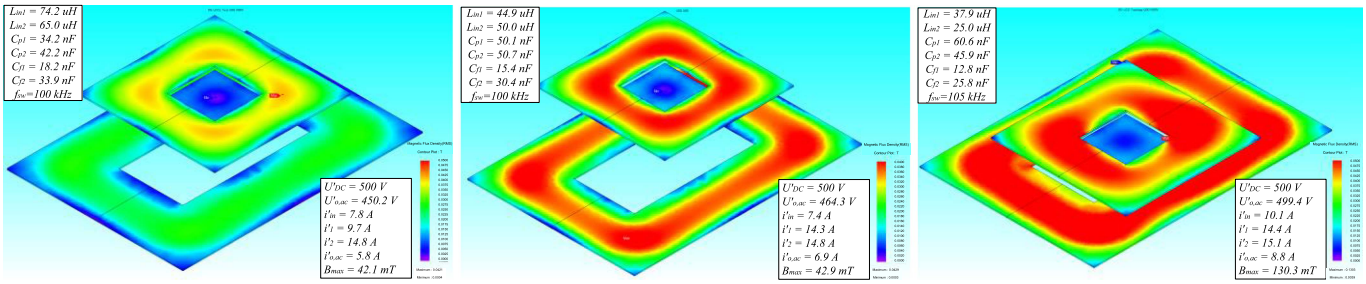

FIGURE 12. 3D FEM simulation results (DS-LCC topology, $U_{DC} = 500$ V) (a) At $z = 100$ mm (align), (b) At $z = 150$ mm, and (c) at $x, y, z = 100$ mm.

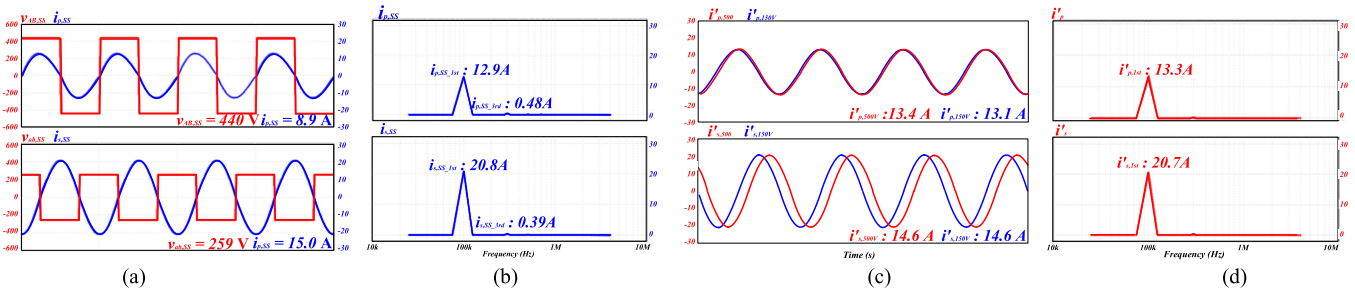

FIGURE 13. PSIM simulation results at $z = 100$ mm: (a) S–S topology, (b) Current component flowing through the coupling pad in S-S topology via Fourier transform, (c) DS-LCC at $U_{DC} = 150$ V, 500 V, (d) Current component flowing through the coupling pad in DS-LCC topology via Fourier transform.

AC current. Fig. 9(c) is the simulation result at $x, y, z = 100$ mm, and the operating frequency is selected at 105-kHz to maintain the output AC current. The input voltage is operated at 290-V after assuming that the duty ratio control is applied in 0.45. The maximum magnetic flux density produced by the coupling pad.

Figs. 13, 14 and 15 show the S-S and DS-LCC topologies in alignment and misalignment, respectively, and the Fourier transform of the current flowing through the coupling pad. The simulation results indicated that DS-LCC topology reconfiguration allowed for flexible variation of the input/output voltage characteristics while applying the same voltage/current stresses to the coupling pad. Figs. 13(b), 14(b) and 15(b) show the fundamental and harmonic components of the current flowing through the coupling pad in the S-S topology. The DS-LCC topology reconfiguration method proposed in this paper measured the voltage/current stresses generated in the rated operation. When applying the rated power, the harmonic component was negligible (less than 5%). Accordingly, when measuring the voltage/current stresses of the coupling pad, applying the FHA was considered reasonable.

B. COMPARISON OF EXPERIMENTAL RESULTS

A 3.3-kW experimental prototype is built, as shown in Fig. 16. The electrical characteristics of the measured coupling pad and the resonance circuit parameters of the DS-LCC are provided in Tables 5 and 6, respectively. The rated output and output current of the existing IPT system to be reconfigured

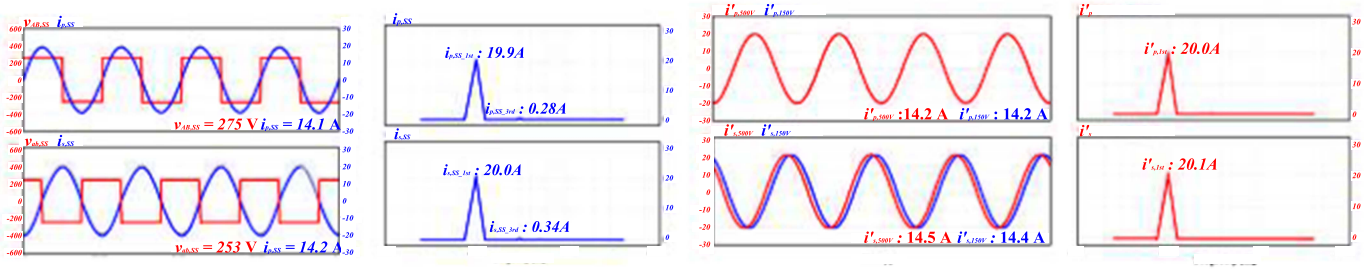

FIGURE 14. PSIM simulation results at z = 150 mm: (a) S–S topology, (b) Current component flowing through the coupling pad in S-S topology via Fourier transform, (c) DS-LCC at UDC = 150 V, 500 V, (d) Current component flowing through the coupling pad in DS-LCC topology via Fourier transform.

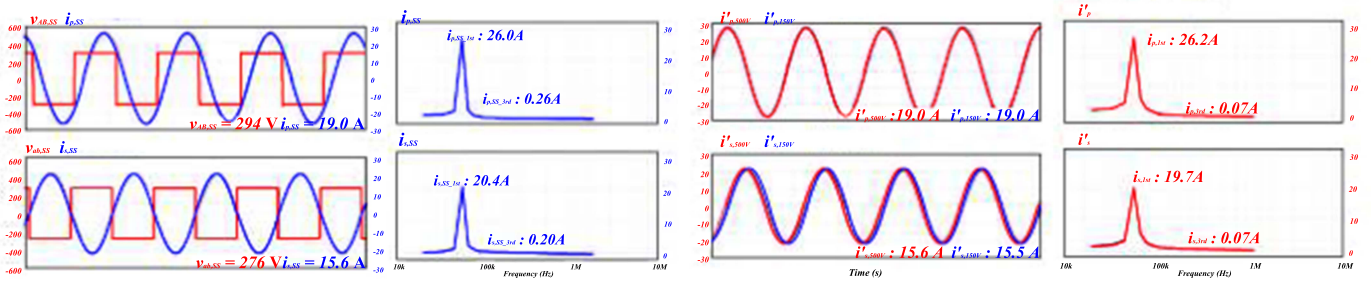

FIGURE 15. PSIM simulation results at x =100 mm, y = 100 mm, z = 100 mm: (a) S–S topology, (b) Current component flowing through the coupling pad in S-S topology via Fourier transform, (c) DS-LCC at U_{DC} = 500 V, (d) Current component flowing through the coupling pad in DS-LCC topology via Fourier transform.

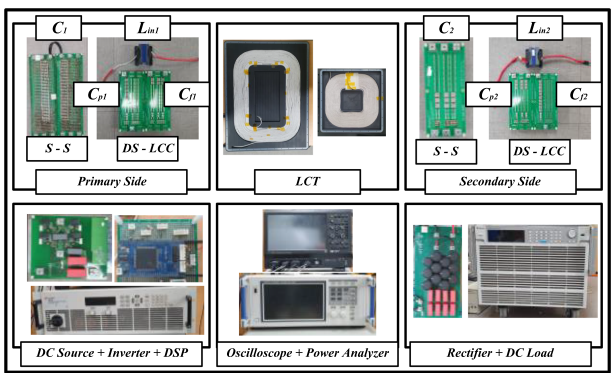

FIGURE 16. Experimental prototype.

TABLE 5. Parameters in the Coupling Pad Prototype

Symbols	Parameters	Values
f_r	Switching frequency	100, 105 kHz
P_o	Rated output power(S-S)	3.3 kW
k	Coupling coefficient range	0.136–0.224
$L_{p,align}$	Primary coil inductance(z = 100mm)	222.5 μH
$L_{s,align}$	Secondary coil inductance(z = 100mm)	160.2 μH
$L_{p,misalign}$	Primary coil inductance(z = 150mm)	226.9 μH
$L_{s,misalign}$	Secondary coil inductance(z = 150mm)	161.7 μH
M	Mutual inductance range	25.6–42.3 μH

TABLE 6. DS-LCC Parameter of Experimental Prototype

Parameters	Values		
	z = 100mm	z = 150mm	x, y, z = 100 mm
L_{in1}	23.96 μH	15.3 μH	15.02 μH
L_{in2}	15.06 μH	15.0 μH	18.04 μH
C_{p1}	168.70 nF	165.3 nF	153.05 nF
C_{p2}	105.35 nF	176.1 nF	128.41 nF
C_{f1}	12.93 nF	12.25 nF	10.85 nF
C_{f2}	17.61 nF	18.35 nF	16.54 nF

are the same as those in Table 4. The output rated characteristics in

Table 4 and the input/output voltage specifications required in the laboratory are assumed to be below 200 V. The MOSFET used in the inverter is C3M0030090K, and the rectifier diode used is IDW40E65D1FKSA1. For the reconfiguration of the DS-LCC topology, the cores of L_{in1} and L_{in2} were made of PC95 material in PQ7261 size. To measure the input and output characteristics, a HIOKI PW6001 power analyzer was used. Additionally, the input and output voltages and currents, as well as the currents in the coupling pads, were measured using an oscilloscope. The input power source was a KEYSIGHT N8955A DC power supply, and the load was applied using the CHROMA 63210E-1200-400 model. The

(a) (b)

FIGURE 17. Experiment results for alignment states: (a) S–S topology and (b) DS-LCC topology.

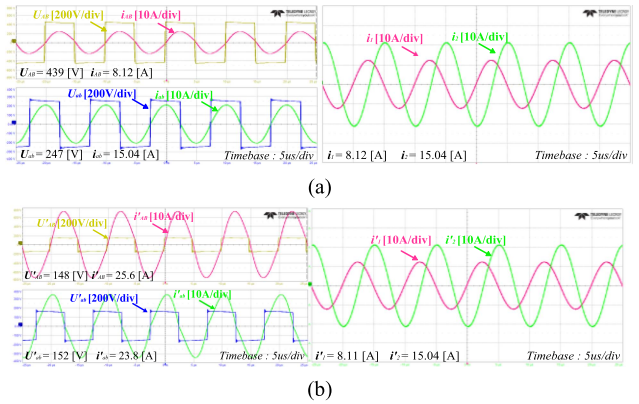

FIGURE 18. Alignment state waveforms with (a) S–S topology and (b) DS-LCC topology.

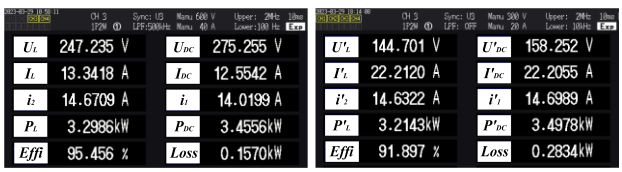

(a) (b)

FIGURE 19. Experiment results for misalignment (vertical) states with DC link control: (a) S–S topology and (b) DS-LCC topology.

input voltage is selected as 440 V, 275 V, and 290 V, respectively, to ensure that the output current of the S-S topology is 13-A during the rated power operation, respectively. The load resistance value is selected as 18.53 Ω to ensure that the output power of the S-S topology is rated at 3.3 kW.

After the S-S topology operation experiment, the DS-LCC is reconfigured and the resonant inductors and capacitors are redesigned. In order to verify that the input voltage and the output voltage can be flexibly designed, the input voltage and the output voltage are designed to be 150-V in the alignment and vertical misalignment states. During the misalignment operation, the coupling pad current measurements of the S-S topology are performed by controlling the DC link voltage, switching frequency, and duty ratio.

Figs. 17 –22 present the experimental results and waveforms, which verify that the input/output characteristics can be flexibly designed through the DS-LCC topology reconfiguration. Figs. 17 and 18 show the results of operating the S-S

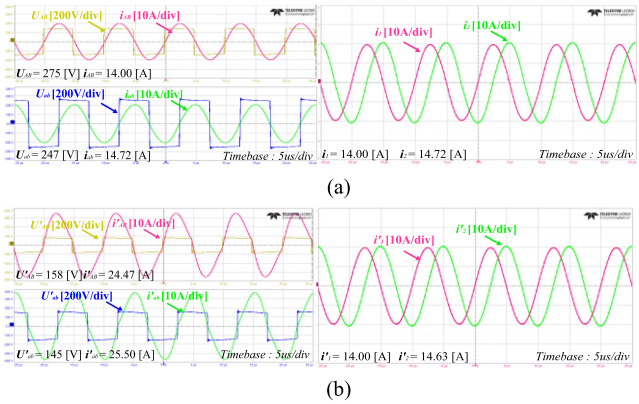

FIGURE 20. Misalignment state(vertical) waveforms with DC link control: (a) S–S topology and (b) DS-LCC topology.

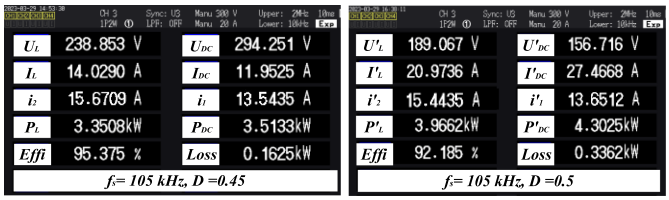

(a) (b)

FIGURE 21. Experiment results for misalignment(horizontal) states with switching frequency and duty control: (a) S–S topology and (b) DS-LCC topology.

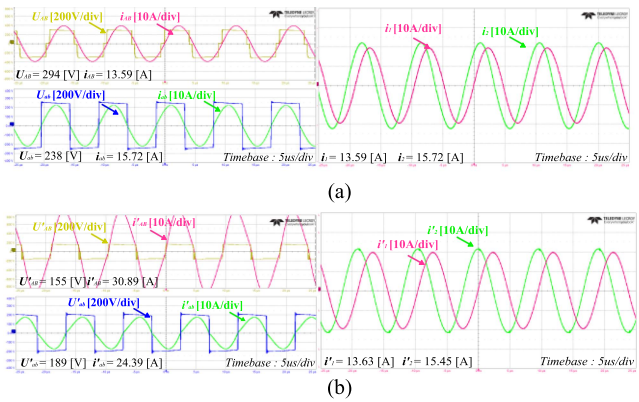

FIGURE 22. Misalignment state(horizontal) waveforms with frequency control: (a) S–S topology and (b) DS-LCC topology.

and DS-LCC topologies in the aligned state. When designing with the S-S topology, 440-V of DC link voltage is required for 3.3-kW rated operation. However, when reconfigured with the DS-LCC topology, the IPT system can operate at less than 200 V.

Through power analyzers and oscilloscope measurements, the i'_p and i'_s are 8.2-A and 15.1 A, respectively.

Figs. 19 and 20 show the results of operating the S-S and DS-LCC topologies in the vertical misalignment state. For

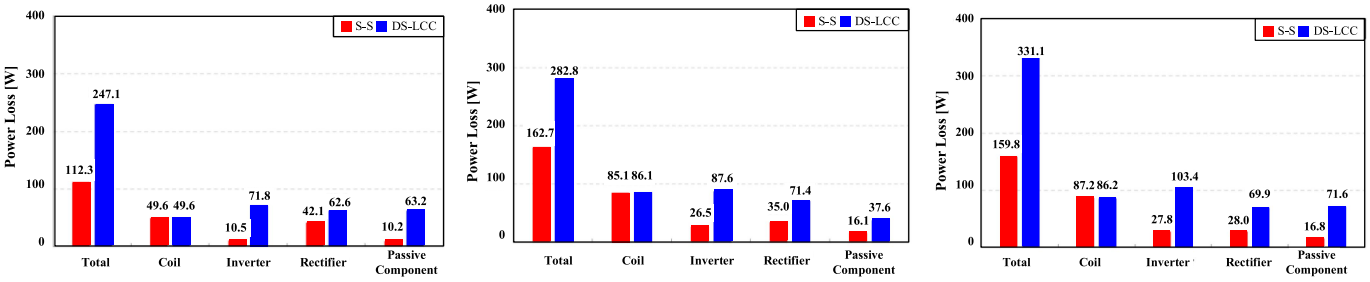

FIGURE 23. Loss distribution for the IPT systems: (a) $z = 100$ mm, (b) $z = 150$ mm, and (c) $x, y, z = 100$ mm.

the same 3.3-kW rated output operation under vertical misalignment, the S-S topology is operated at 275 V. Moreover, when reconfigured with the DS-LCC topology, the IPT system designed the resonance element value to operate at 150 V. From the power analyzer and oscilloscope measurements, the i'_p and i'_s are 14.0-A and 14.6 A, respectively.

Figs. 21 and 22 show the results of operating the S-S and DS-LCC topologies in the horizontal misalignment state. When there is a horizontal separation distance, the coupling pad inductance value fluctuated, resulting in input phase fluctuations. For the S-S topology to maintain the ZVS phase, the rating test was conducted by controlling the DC link (295-V), operating frequency (105 kHz), and duty (0.45). When reconfiguring the DS-LCC topology, the operating frequency affected the iron losses. Therefore, the frequency is selected as 105 kHz, and the i'_p and i'_s are calculated and tested based on Fig. 4. The experimental test results are confirmed that i'_p is 13.6-A and i'_s is 15.6-A while achieving the input voltage of 156-V and the output voltage of 189 V. From these three experiments, it confirms that the DS-LCC topology reconfiguration method can be used for measurements by applying the same current stress to the coupling pad, regardless of the input/output voltage specification.

C. SYSTEM LOSSES AND TEMPERATURE MEASUREMENTS

The losses incurred when reconfigured with the DS-LCC topology and the IPT system configured with the S-S topology for development were different depending on the differences in input/output characteristics and the resonance network configuration.

Fig. 23 shows a graph of the loss configuration of IPT system. The gate driver and controller were powered by a separate DC power supply, independent of the main system, to exclude their losses from the overall measurements. The losses in the inverter and rectifier were calculated based on the MOSFET's switching losses, conduction losses, and the diode forward power losses, respectively. The passive component losses were calculated as the sum of the core losses of a PQ7261 size inductor, the copper losses of the inductor winding, and the equivalent series resistance of resonant capacitors. Since DS-LCC has lower voltage input and output characteristics, the DS-LCC topology has higher inverter and rectifier losses in the process of sending the same power. Moreover, different from the S-S topology, an additional loss occurred in the resonant inductor. The experiments confirmed that the total loss from the coupling pad was almost the same.

Table 7 compares the temperature changes of the coupling pad when operating the IPT system consisting of the S-S topology and the DS-LCC topology for 30-minute in the

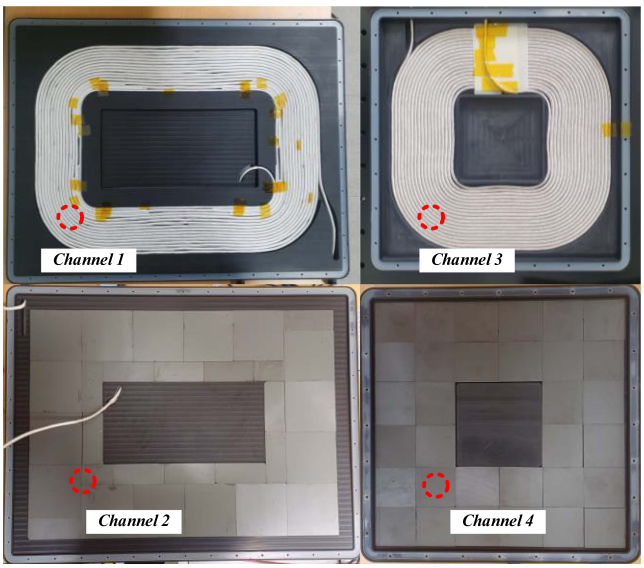

FIGURE 24. Temperature sensor channel position in coupling pad.

TABLE 7. Temperature Change With 30-Minute Operation

Channel	*Position*	*Topology*	*Start*	*30 min*	*Difference*
Channel 1	Primary Coil	S-S	24.5	31.6	7.1
		DS-LCC	24.9	32.1	7.2
Channel 2	Primary Magnetic	S-S	24.7	33.5	8.8
		DS-LCC	25.2	34	8.8
Channel 3	Secondary Coil	S-S	24.2	28.6	4.4
		DS-LCC	24.9	29.2	4.3
Channel 4	Secondary Magnetic	S-S	23.6	27.7	4.1
		DS-LCC	23.9	28.7	4.8

aligned state. The heat dissipation was achieved through natural air cooling without any additional cooling equipment. The position of each temperature sensor channel, attached in areas where the magnetic flux density is concentrated, is specified in Fig. 24.

Table 7 confirms that the temperature increase is almost the same. Therefore, the proposed measurement method is considered reasonable for verifying the voltage/current stresses and losses generated in the coupling pad through the DS-LCC topology reconfiguration.

V. CONCLUSION

This paper presents a novel method for reconfiguring the DS-LCC topology to achieve consistent coupling pad stress measurement and validation, regardless of the electrical specifications of the input/output equipment. The rated operational electrical characteristics of the input, output, primary, and secondary coupling pads across various compensation topologies were analyzed, and DS-LCC topology parameters were designed to achieve ZVS of the inverter while applying the same pad current stress. This provides flexibility to accommodate the voltage and current constraints of input/output equipment. Simulation and experimental results confirmed that the coupling pad stress characteristics, losses, and temperature rise trends are similar.

The proposed reconfiguration method is applicable to various IPT applications and can significantly reduce the time and cost for researchers and developers in setting up hardware and software infrastructure. This allows for proactive adaptation to rapidly changing IPT system specifications, such as increased battery rated voltage and changes in input voltage due to single-phase/three-phase alterations. However, since the proposed measurement method only measures the rated stress at specific locations, it is recommended to use the reconfiguration method in situations where the coupling pad experiences the highest stress (e.g., increased operating frequency, increased coupling pad current).

In conclusion, the proposed DS-LCC topology reconfiguration method is useful for verifying issues that may arise in coupling pads during rated power tests applied to various applications in limited laboratory environments. This contributes significantly to the advancement of wireless power transfer technology and the resolution of engineering challenges.

APPENDIX

In addition to the S-S topology exemplified in this paper, the PSIM simulation results for the DS-LCC topology reconfiguration with the LCC-S topologies is provided as examples. Fig. 25 along with Tables 8 and 9 demonstrate that the LCC-S topologies can also apply the same current stress through the DS-LCC topology reconfiguration.

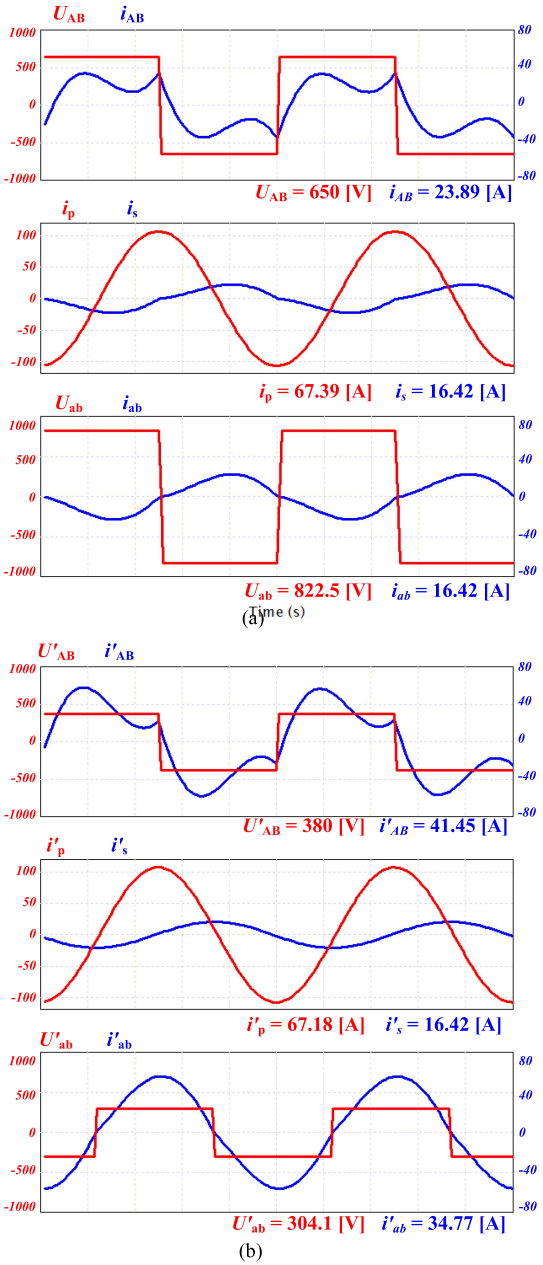

FIGURE 25. PSIM simulation waveforms for the DS-LCC topology reconfiguration with the LCC-S topology: (a) LCC-S topology and (b) DS-LCC topology reconfiguration.

TABLE 8. Parameters in the LCC-S Topology

Symbols	Parameters	Values
U_{DC}	DC input voltage	650 V
U_L	DC output voltage	830 V
f_r	Switching frequency	100 kHz
P_L	Rated output power(LCC-S)	11 kW
k	Coupling coefficient range	0.2
L_{pA}	Primary coil inductance	60 μH
L_{sA}	Secondary coil inductance	100 μH
L_{in}	Resonant inductor	12.132 μH
C_p	Primary parallel capacitor	208.78 nF
C_f	Primary series capacitor	52.92 nF
C_s	Secondary series capacitor	25.33 nF

TABLE 9. DS-LCC Reconfiguration Parameters

Parameters	Values	Parameters	Values
U'_{DC}	380 V	C_{p1}	357.13 nF
U'_{L}	304 V	C_{p2}	84.43 nF
L_{in1}	7.09 μH	C_{f1}	47.88 nF
L_{in2}	30 μH	C_{f2}	36.19 nF

REFERENCES

[1] A. P. Sample, D. T. Meyer, and J. R. Smith, "Analysis, experimental results, and range adaptation of magnetically coupled resonators for wireless power transfer," *IEEE Trans. Ind. Electron.*, vol. 58, no. 2, pp. 544–554, Feb. 2011.

[2] G. A. Covic and J. T. Boys, "Modern trends in inductive power transfer for transportation applications," *IEEE J. Emerg. Sel. Topics Power Electron*, vol. 1, no. 1, pp. 28–41, Mar. 2013.

[3] J. H. Kim et al., "Development of 1-MW inductive power transfer system for a high-speed train," *IEEE Trans. Ind. Electron.*, vol. 62, no. 10, pp. 6242–6250, Oct. 2015.

[4] M. Sugino and T. Masamura, "The wireless power transfer systems using the Class E push-pull inverter for industrial robots," in *2017 IEEE Wireless Power Transfer Conf.*, Taipei, 2017, pp. 1–3.

[5] P. K. Chittoor, B. Chokkalingam, and L. Mihet-Popa, "A review on UAV wireless charging: Fundamentals, applications, charging techniques and standards," *IEEE Access*, vol. 9, pp. 69235–69266, 2021.

[6] F. Freschi, M. Mitolo, and R. Tommasini, "Electrical safety of plug-in electric vehicles: Shielding the public from shock," *IEEE Ind. Appl. Mag.*, vol. 24, no. 3, pp. 58–63, May/Jun. 2018.

[7] B. Wang, P. Dehghanian, S. Wang, and M. Mitolo, "Electrical safety considerations in large-scale electric vehicle charging stations," *IEEE Trans. Ind. Appl.*, vol. 55, no. 6, pp. 6603–6612, Nov./Dec. 2019.

[8] X. Dai, X. Li, Y. Li, and P. Hu, "Maximum efficiency tracking for wireless power transfer systems with dynamic coupling coefficient estimation," *IEEE Trans. Power Electron.*, vol. 33, no. 6, pp. 5005–5015, Jun. 2018.

[9] H. Yang et al., "A hybrid load matching method for WPT systems to maintain high efficiency over wide load range," *IEEE Trans. Transp. Electrific.*, vol. 9, no. 1, pp. 1993–2005, Mar. 2023.

[10] Siyuan Lu, Mike Böttigheimer, and Nejila Parspour, "An impedance mapping-based T-Compensation network and control strategy for WPT System with full-bridge active rectifier," *IEEE Trans. Power Electron.*, vol. 38, no. 11, pp. 14675–14688, Nov. 2023.

[11] I. -W. Iam, C. -K. Choi, C. -S. Lam, P. -I. Mak, and R. P. Martins, "A constant-power and optimal-transfer-efficiency wireless inductive power transfer converter for battery charger," *IEEE Trans. Ind. Electron.*, vol. 71, no. 1, pp. 450–461, Jan. 2024.

[12] P. Vishnuram et al., "Review of wireless charging system: Magnetic materials, coil configurations, challenges, and future perspectives," *Energies*, vol. 16, 2023, Art. no. 4020.

[13] R. Tanzania, F. H. Choo, and L. Siek, "Design of WPT coils to minimize AC resistance and capacitor stress applied to SS-topology," in *Proc. 41st Annu. Conf. IEEE Ind. Electron. Soc.*, Nov. 2015, pp. 118–122.

[14] A. A. S. Mohamd, S. An, and O. Mohammed, "Coil design optimization of power pad in IPT system for electric vehicle applications," *IEEE Trans. Magn.*, vol. 54, no. 4, Apr. 2018, Art. no. 9300405.

[15] M. -H. Kang, J. Byeon, D. -M. Joo, M. Kim, and B. K. Lee, "Design of optimum self-inductances of magnetic pads in inductive power transfer system for electric vehicles," in *2016 IEEE Energy Convers. Congr. Expo.*, Milwaukee, WI, USA, 2016, pp. 1–5.

[16] D. E. Gaona and T. Long, "Feasibility analysis of nanocrystalline cores for polarize and non-polarized IPT charging pads," in *2019 IEEE Appl. Power Electron. Conf. Expo.*, Anaheim, CA, USA, 2019, pp. 1539–1546.

[17] T. Noda, T. Nagashima, and H. Sekiya, "A design of inductively coupled wireless power transfer system with coupling coil optimization," in *Proc. IEEE Int. Telecommun. Energy Conf.*, Oct. 2015, pp. 1–6.

[18] G. Wei, X. Jin, C. Wang, J. Feng, C. Zhu, and M. I. Matveevich, "An automatic coil design method with modified AC resistance evaluation for achieving maximum coil–Coil efficiency in WPT systems," *IEEE Trans. Power Electron.*, vol. 35, no. 6, pp. 6114–6126, Jun. 2020.

[19] S. Kim, H. -H. Park, J. Kim, J. Kim, and S. Ahn, "Design and analysis of a resonant reactive shield for a wireless power electric vehicle," *IEEE Trans. Microw. Theory Techn..*, vol. 62, no. 4, pp. 1057–1066, Apr. 2014.

[20] M. Lu and K. D. T. Ngo, "A fast method to optimize efficiency and stray magnetic field for inductive-power-Transfer coils using lumped-loops model," *IEEE Trans. Power Electron.*, vol. 33, no. 4, pp. 3065–3075, Apr. 2018.

[21] Y. Chen, H. Zhang, S. -J. Park, and D. -H. Kim, "A switching hybrid LCC-S compensation topology for constant current/voltage EV wireless charging," *IEEE Access*, vol. 7, pp. 133924–133935, 2019.

[22] Z. Dai and J. Wang, "A dual-frequency WPT based on multilayer self-decoupled compact coil and dual CLCL hybrid compensation topology," *IEEE Trans. Power Electron.*, vol. 37, no. 11, pp. 13955–13965, Nov. 2022.

[23] W. Hurley, E. Gath, and J. Breslin, "Optimizing the AC resistance of multilayer transformer windings with arbitrary current waveforms," *IEEE Trans. Power Electron.*, vol. 15, no. 2, pp. 369–376, Mar. 2000.

[24] J. Reinert et al., "Calculation of losses in ferro- and ferrimagnetic materials based on the modified Steinmetz equation," *IEEE Trans. Ind. Appl.*, vol. 37, no. 4, pp. 1055–1061, Jul./Aug. 2001.

[25] R. L. Steigerwald, "A comparison of half-bridge resonant converter topologies," *IEEE Trans. Power Electron.*, vol. 3, no. 2, pp. 174–182, Apr. 1988.

[26] V. Shevchenko, O. Husev, R. Strzelecki, B. Pakhaliuk, N. Poliakov, and N. Strzelecka, "Compensation topologies in IPT systems: Standards, requirements, classification, analysis, comparison and application," *IEEE Access*, vol. 7, pp. 120559–120580, Aug. 2019.

[27] W. Zhang and C. C. Mi, "Compensation topologies of high-power wireless power transfer systems," *IEEE Trans. Veh. Technol.*, vol. 65, no. 6, pp. 4768–4778, Jun. 2016.

[28] Z. Liu, L. Wang, Y. Guo, and S. Li, "Primary-side linear control for constant current/voltage charging of the wireless power transfer system based on the LCC-N compensation topology," *IEEE Trans. Ind. Electron.*, vol. 69, no. 9, pp. 8895–8904, Sep. 2022.

[29] Y. Zhang et al., "A hybrid compensation topology with constant current and constant voltage outputs for wireless charging system," *IEEE Trans. Transp. Electrific.*, vol. 9, no. 2, pp. 2070–2080, Jun. 2023.

[30] S. Li, W. Li, J. Deng, T. D. Nguyen, and C. C. Mi, "A double-sided LCC compensation network and its tuning method for wireless power transfer," *IEEE Trans. Veh. Technol.*, vol. 64, no. 6, pp. 2261–2273, Jun. 2015.

[31] SAE International, *Wireless Power Transfer for Light-Duty Plug-In/Electric Vehicles and Alignment Methodology*, Standard SAE J2954, 2020.